REVISION 1:

Timescales of spherulite crystallization in obsidian inferred from water concentration profiles

Jonathan M. Castro[1], Pierre Beck[2], Hugh Tuffen[3], Alexander R.L. Nichols[4], Donald B. Dingwell[5], and Michael C. Martin[6]

ABSTRACT

We determined the kinetics of spherulite growth in obsidians from Krafla volcano, Iceland. We measured water concentration profiles around spherulites in obsidian by Synchotron Fourier Transform Infrared Spectroscopy. The distribution of OH^- groups surrounding spherulites decreases exponentially away from the spherulite-glass border, reflecting expulsion of water during crystallization of an anhydrous paragenesis (plagioclase+SiO_2+clinopyroxene+magnetite). This pattern is controlled by a balance between the growth rate of the spherulites and the diffusivity of hydrous solute in the rhyolitic melt.

We modeled advective and diffusive transport of the water away from the growing spherulites by numerically solving the diffusion equation with a moving boundary. Numerical models fit the natural data best when a small amount of post-growth diffusion is incorporated in the model. Comparisons between models and data constrain the average spherulite growth rates for different temperatures and highlight size-dependent growth among a small population of spherulites.

KEYWORDS: spherulite, diffusion, obsidian, crystallization

[1] Department of Mineral Sciences, Smithsonian Institution, MRC-119, Washington, DC 20013
[2] Laboratoire de Planetologie de Grenoble, 122 rue de la Piscine, Grenoble 38041, France
[3] Environmental Science Department, Lancaster University, Lancaster, UK
[4] Institute for Research on Earth Evolution (IFREE), Japan Agency for Marine Earth Science and Technology (JAMSTEC), 2-15 Nasushima-cho, Yokosuka, Kanagawa 237-0061, Japan
[5] Earth and Environmental Sciences, LMU-University of Munich, Theresienstr. 41/III, 80333Munich, Germany
[6] Advanced Light Source, Lawrence Berkeley National Laboratory, Berkeley, California

INTRODUCTION

The rates and timescales of magmatic processes exert first-order control over the behavior of magmatic systems. For example, the rate of decompression during magma ascent may dictate the manner in which volatiles are released from the melt, ultimately influencing degassing and the explosivity (e.g., Gonnermann and Manga 2007). Similarly, crystallization in volcanic conduits and lava flows may generate excess volatile pressure, leading to nonlinear extrusion and endogenous dome explosions (e.g., Sparks 1997). Clearly, our ability to model magmatic processes depends on accurate determinations of timescales of processes such as crystallization and bubble growth.

Direct measurement of the timing and duration of magmatic phase changes (e.g., crystallization) is challenging due to the extreme inaccessibility of magmatic environments; efforts to do so have been relegated to analyzing natural crystal chronometers in quenched rocks. Crystal size distribution (CSD) analysis for example (e.g., Cashman 1988), has provided estimates of crystal growth rates in magmatic systems. However, temporal information based on CSD interpretations may be subject to large errors, owing to the uncertainties of the underlying governing crystal growth laws, including assumptions that the growth rates of all crystals was the same.

Advances in timescale determinations have been made by analyzing chemical gradients within crystals (Costa and Dungan 2005) and glasses (Castro et al. 2005) combined with diffusion modeling of the elemental distributions. Here, we build on these studies by determining the crystallization timescales of small spherical crystal aggregates in obsidian, known as spherulites (Fig. 1). We present Synchotron Fourier Transform Infrared Spectroscopic (SFTIR) measurements of water concentration profiles

around spherulites in obsidian. We then model the concentration profiles by numerically solving the advection-diffusion equation for a range of temperatures to yield model crystallization timescales.

GEOLOGICAL BACKGROUND

Spherulites are radiating, often concentrically arranged aggregates of one or more anhydrous minerals set in a glassy matrix (Fig. 1). They occur in obsidian domes, large-volume vitrophyric ash-flow tuffs (e.g., Smith et al. 2001), and in shallow volcanic conduits (e.g., Stasiuk et al. 1996). Spherulites are inferred to have nucleated and grown in response to large undercoolings (> 200˚C) rapidly imposed on the magma by its degassing and quenching (e.g., Swanson et al., 1989). As dictated by the thermal profile of the magma body (Manley 1992), spherulitic obsidian develops in spatially restricted zones (e.g., Manley and Fink 1987; Stevenson et al. 1994), comprising a transitional facies that separates the rapidly quenched, outermost vitrophyric rhyolite from a devitrified microcrystalline core.

Anomalously high volatile contents exist within and just above the spherulitic zones in lava domes (e.g., Westrich et al. 1988). Several authors have suggested a genetic link between spherulite crystallization and the increase in volatile pressure within lava domes (e.g., Wright 1915), although to date there is only circumstantial evidence supporting such a “second boiling” phenomenon (Manley and Fink 1987). Below we present the first direct evidence for water concentration gradients around spherulites. We use this information to quantitatively estimate the kinetics of spherulite growth.

SAMPLES AND METHODS

89 Decimeter-sized rhyolitic obsidian samples were collected from the
90 Hrafntinnuhryggur ridge system on Krafla volcano, Iceland. These obsidians come from
91 a small (~5 m tall) outcrop that is part of an elongate series of domes marking the roof of
92 a dike that intruded an ice sheet (Tuffen and Castro, in preparation). Doubly polished
93 wafers, 100-200 μm thick were prepared from 5 obsidian samples. The spherulites are
94 numerous, mostly spherical, randomly spaced, and of a limited size (~50-800 μm). As a
95 result, the intersection planes of the wafers commonly expose 1 to 3 spherulites along
96 their maximum (equatorial) dimension. Using this geometry, we have been able to relate
97 the variation in H_2O species to the radial growth direction of the spherulites.
98 H_2O concentrations were determined by SFTIR at the Advanced Light Source,
99 Lawrence Berkeley National Laboratory. Measurements were made along traverses
100 oriented perpendicular to the spherulite-glass boundaries on a Thermo Nicolet Magna
101 760 FTIR spectrometer interfaced with a NicPlan IR microscope (at beamline 1.4.3). The
102 IR beam has a diffraction-limited diameter of about 3 μm. The uncertainty in spot
103 position is $\pm$ 2 μm. Transmittance spectra were obtained over the mid-IR (1,400-4,000
104 cm-1) to the near-IR (3,700-6,500 cm^{-1}) regions with MCT detectors, KBr beam-splitters,
105 and the synchotron light source. 128 scans were used to obtain each spectrum and these
106 spectra were corrected by subtracting a background spectrum collected every hour. We
107 determined OH^- concentrations from the intensity of the broad 3,570 cm^{-1} absorption
108 band, utilizing an absorption coefficient of 100 L mol•cm^{-1} (Newman et al. 1986). We
109 estimate the analytical uncertainty of OH- concentration to be $\pm$ 10% of the measured
110 value.

Spherulite mineralogy was determined by 1) microscopic observation, 2) sample magnetism to identify Fe-oxides as magnetite, and 3) compositional data from energy dispersive spectra (EDS) collected on a Field-Emission SEM at the Smithsonian Institution National Museum of Natural History. The SEM was operated at 10-12 KeV, 1 mm working distance and beam current ranging from 0.5-1 nanoamps. Precise identification of spherulite minerals was challenging due to the small size (often < 2 μm) of individual phases (Fig. 1) and their intimate, interlocking growth habits (Fig. 2), which invariably resulted in the electron beam sampling parts of neighboring phases. However, where possible, we analyzed the largest regions of a continuous phase. Mineralogic determinations were made based on the peaks that appeared in the EDS specta; minor peaks nested within the background radiation were not used to infer mineralogy.

The glass transition temperature of the Krafla obsidian was determined by differential scanning calorimetry using a Netzsch DSC 404C at the University of Munich following the procedure of Gottsmann et al. (2002).

Glass compositions were analyzed using a JEOL JXA-8900R electron microprobe (EPMA) running software with ZAF corrections at the Smithsonian National Museum of Natural History. Analyses were performed with an acceleration voltage of 15 keV, a 10 μm beam, and a 10 nA beam current. Standardization was performed on the following natural mineral standards: Quartz (Si), Anorthite (Ca), Bytownite (Al), Microcline (K), Albite (Na), Hornblende (Fe, Mg). A natural rhyolitic glass (VG568) of known major element composition was periodically analyzed to check for instrument drift.

ANALYTICAL RESULTS

133 Spherulites consist of, in order of modal abundance, sodic plagioclase (~45%), an
134 SiO_2-polymorph, quite possibly quartz (~40%), clinopyroxene (~3%) and magnetite (~1-
135 2%; Fig. 2). In addition, the largest spherulites (>500 μm) contain a small amount (<15
136 vol.%) interstitial glass and microvesicles (<1 vol.%). This phase assemblage accounts
137 for most of the major elements analyzed on bulk samples of the Krafla rhyolite (Table 1),
138 however, potassium appears to have behaved incompatibly during spherulite
139 crystallization as it was not detected in any of the phases. Like water, potassium is
140 probably concentrated in the surrounding glass matrix.
141 The plagioclase and the SiO_2-polymorph textures (Figs.1, 2) mimic micrographic,
142 micropoikilitic, and granophyric intergrowths observed in nature and produced
143 experimentally (e.g., MacLellan and Trembath, 1991). In both cases, the SiO_2-phase
144 often hosts plagioclase microlites.
145 Spherulites are typically enclosed in haloes of colorless rhyolitic glass (Table 1),
146 which separate them from the pervasive brown matrix glass (Fig. 1). Glass color
147 differences correspond to different oxidation states of iron (Galliard et al. 2003). In
148 cross-polarized light, the colorless glass regions are birefringent, as evidenced by their
149 first-order grey color (Fig. 1b). Spherulites commonly overprint pyroxene- and Fe-oxide
150 microlite-defined flow banding, however, in one sample, microlites are deflected around
151 the spherulites (Fig. 1c).
152 Figure 3 shows a subset of OH^- concentration profiles; the complete analytical
153 data are reported in Table 2. The area under the OH^- concentration profiles is
154 proportional to the amount of water surrounding each spherulite that is elevated above the
155 far-field matrix concentration. We quantified this water enrichment by fitting the OH^-

concentration profiles with polynomials and then integrating from the point of maximum OH^- content to the far-field matrix value (Table 2). We then subtracted the area corresponding to the background water concentration from the total area under the curve to get the amount of water in excess of the far-field value. Concentrations were converted from wt.% to milligram units by multiplying the volume of glass having elevated water by a glass density of 2.326 g cm^{-1}, determined from the major element chemistry of the glass (Table 1) using the method of Ghiorso and Sack (1995). The resultant mass of glass was then multiplied by the weight fraction of OH^- measured in the elevated region.

The amount of water surrounding spherulites increases with the spherulite size, and in most cases, matches the amount of water that would be expulsed during complete crystallization of anhydrous minerals from a volume of melt equal to the volumes of each spherulite (Table 2), as determined by their radii. Differences between the measured and predicted water show that some spherulites retained water during their growth (e.g., as seen in OR1305_A), consistent with the presence of a small amount of glass and microvesicles in some of them.

SPHERULITE CRYSTALLIZATION KINETICS

It is clear from the mass-volume balance between the OH^- concentrations and the corresponding volume of the spherulites that the concentration profiles were produced by the rejection of water during the growth of anhydrous minerals in the spherulites. As the spherulites grew and expelled water outwardly, the flux of water at the spherulite edge was counter balanced by diffusion of water away from the spherulite-melt/glass

boundary. Thus, spherulite growth (ie., advection) and diffusion worked in concert to produce the natural water concentration profiles.

By modeling the combined growth and diffusion processes, and comparing model and natural water concentration profiles, we can estimate timescales of spherulite growth. Specifically, we solved numerically the advection-diffusion equation in spherically symmetrical form within the reference frame of the moving spherulite-melt/glass boundary (Crank, 1984):

$$\frac{\partial C}{\partial t} + u \cdot \frac{\partial C}{\partial r} = D(C,T,P)\left(\frac{\partial^2 C}{\partial r^2} + \frac{2}{r} \cdot \frac{\partial C}{\partial r}\right), \quad (r > r_i) \qquad (1)$$

Here, t is time, r is the spherulite radius, r_i is the crystal/melt interface position, C is the concentration of OH^- species, and D is the diffusivity of H_2O in the melt. We note that even though OH^- is the dominant hydrous species measured in these obsidians, hydrous species diffusion likely occurs through the migration of molecular H_2O (e.g., Zhang et al. 1991). Consequently, our model calculates the diffusivity of molecular H_2O, which changes with T, P, and C according to the formula of Zhang and Behrens (2000).

The second term on the LHS of equation 1 represents advection, and requires the choice of a spherulite growth law that will dictate the velocity of the spherulite-matrix interface, u or $\frac{dr_i}{dt}$. This velocity, in turn, determines the flux of water extruded from the moving boundary after each time step.

The form of the spherulite growth law is an *a priori* unknown function of time. We assume that the growth rate decreased exponentially with time; this assumption is justified for the case that growth was limited by the diffusion rates of crystal nutrients

200 towards the growth boundary, and possibly by diffusion of hydrous species and other
201 impurities away from the boundary (e.g., Frank, 1950; Keith and Padden, 1964; Granasy
202 et al., 2005). We chose the following exponential growth law:

203 $$\frac{dr_i}{dt} = R\frac{2}{\sqrt{\pi}}\exp\left[-\left(\frac{t}{\tau}\right)^2\right], \quad (2)$$

204 where the parameter τ is the spherulite growth timescale and the primary fitting
205 parameter, and R is the spherulite radius.

206 The numerical model calculates by finite difference the amount of water released
207 at the spherulite-matrix boundary per each increment of growth; the amount of water
208 ejected is determined by mass conservation at the boundary:

209 $$\left(\int_0^L 4\pi r^2 C(r)dr\right)_{t=0} = \left(\int_{r_i}^L 4\pi r^2 C(r)dr\right)_t, \quad (3)$$

210 where, L is the width of the matrix. The initial water concentration prior to spherulite
211 growth is the average OH^- value measured in the "far field" along the flat part of the
212 profile. In the model, mass transport takes place solely in the radial direction away from
213 the interface (Fig. 4).

214 The modeling routine involves varying the growth timescale (τ), which is the
215 amount of time that the model runs to reach the target spherulite radius, iteratively to
216 produce the best fit to the natural data. Other model input parameters include the
217 measured spherulite size, a fixed temperature, and P=0.1 MPa. As the temperature is not
218 well constrained, we have modeled a range of bracketing temperatures (see discussion
219 below). The model does not account for the latent heat of crystallization.

220 We assume that the natural water profiles developed largely during spherulite
221 growth. However, there is evidence that water continued to diffuse after the interface had

222 stopped moving, namely in the form of the profile inflection points, manifested as
223 downturns in the concentration near the spherulite-glass border. These points may arise
224 because the flux of water from the spherulite shuts off when growth ceases, yet diffusion
225 of water due to the concentration gradient at the spherulite margin may continue.
226 Our model accounts for post-growth diffusion by calculating the concentration
227 profile under a no-flux boundary condition after the spherulite grows to its final size. The
228 amount of post-growth diffusion is not known *a priori*. However, because we are
229 interested in determining *maximum* spherulite growth timescales, we ran models with the
230 smallest amount of post-growth diffusion that would properly fit the profiles. We found
231 that a minimum of 6% (ie., 6% of the growth timescale) post-growth diffusion was
232 required to best fit the natural data. Model simulations with < 6% post-growth diffusion
233 did not produce a large enough downturn in the concentration profile, while simulations
234 incorporating more post-growth diffusion required shorter spherulite growth timescales
235 (ie., less syn-growth diffusion).
236 Figure 4b shows an example of a calculation with and without post-growth
237 diffusion; the model with post-growth diffusion reproduces the downturn near the
238 spherulite-glass border and the natural sigmoidal concentration profile shapes well.
239 The crystallization temperature is an unknown. The observation that spherulites
240 deflect the banding in some samples (Fig. 1c) indicates that crystallization may have
241 begun above the glass transition temperature (T_g), where the melt was capable of viscous
242 deformation. In most samples however, spherulites overprint banding; thus their growth
243 must have continued after that viscous deformation had ceased. Evidence that spherulite
244 growth continued below T_g includes the birefringent haloes (Fig. 1b). Birefringence

245 reflects anisotropy in the glass, which results from unrelaxed stress accumulation during
246 hydration as the spherulites grew (e.g., Friedman and Smith 1960). The preservation of
247 anisotropy, therefore, shows that some of the growth took place below T_g, otherwise, the
248 expansion of the melt structure due to hydration would have been accommodated by
249 flowage of the melt around the hydrous region and subsequent strain relaxation in the
250 hydrous zone.

251 Differential scanning calorimetric measurements constrain T_g of these obsidians
252 to be about 690˚C (±20˚C). Because our diffusion model only operates at a fixed
253 temperature, we modeled spherulite growth near the glass transition, at 700˚C, in addition
254 to bracketing temperatures of 650˚, 800˚, and 850˚C. The resultant diffusion curves were
255 superimposed on the natural data (Fig. 4c). The best-fit growth timescales were then
256 converted to average linear growth rates by dividing the growth timescale by the
257 observed spherulite size (Table 3). Average growth linear growth rates are minimum
258 values, and are used solely to compare model results at different temperatures and to
259 examine possible variations in growth rate with spherulite size.

260 Spherulite growth timescales range from about 1 day to nearly 2 weeks depending
261 on the temperature (Fig. 5a; Table 3). The growth timescale of the largest spherulite
262 (OR1305_A) is discordant, probably because this spherulite had retained water during its
263 growth (Table 3). In this case, the profile (Fig. 3a) appears to be more evolved than it
264 actually is, and a longer diffusion time was required to properly fit the profile (complete
265 profile data is available in an electronic supplement).

266 Spherulite growth timescales are remarkably consistent at each model temperature
267 (Table 3). This finding makes geological sense, in that the spherulites come from a

268 relatively small region of melt, one that would have experienced roughly the same
269 cooling rate. Gottsmann and Dingwell (2001) determined the cooling rates of
270 compositionally similar spherulitic obsidians to be about ~ 0.003-0.0006 ˚C s^{-1}, implying
271 timescales of about 20 to 100 hours to cool from 850 to 650 ˚C. This cooling interval
272 falls within the range of spherulite growth timescales determined from the concentration
273 profiles, and thus, provides an independent check on our results.
274 Spherulite growth rates calculated from growth timescales vary by about one
275 order of magnitude (~10^{-10}-10^{-9} m s^{-1}) across the 200˚C range of temperature (Fig. 5b).
276 These data define a range of permissible growth rates in the event that cooling was
277 important during spherulite growth. For example, if a spherulite began to grow at 800˚C
278 and stopped growing at 700˚C, then the effective average growth rate would be
279 intermediate to the bounding isothermal-model-derived values, as cooling would cause
280 the growth rate to slow down from the value at 800˚C.
281 The average growth rates closely match the values determined experimentally in
282 model orthoclase-quartz eutectic melts (~10^{-10}-10^{-9} m s^{-1}; Baker and Freda, 2001). By
283 contrast, the growth rates determined herein exceed the values determined experimentally
284 in synthetic water-saturated rhyolite melts (~10^{-13}-10^{-11} m s^{-1}; Swanson 1977).
285 Interpreting our results in the context of experimental studies is not warranted beyond
286 these simple comparisons due to the fact that several variables in the natural system, such
287 as temperature, are not precisely known.
288 With the exception of the largest spherulite (OR1305_A), the average growth
289 rates increase linearly with spherulite size at a given temperature, reflecting size-
290 dependent growth (Fig. 5). Size-dependent crystal growth has been observed in

crystallization experiments (Randolf and Larson 1988). In such experiments, larger crystals typically grow faster than smaller ones. It has also been observed that equal-sized crystals in close proximity to one another may grow at disparate rates. Apart from the data presented in this paper, these phenomena have not been documented in natural systems; however, size-dependent and dispersive growth have been proposed as mechanisms to generate lognormal crystal size distributions common in igneous rocks (e.g., Eberl et al. 2002). That individual spherulites may grow at different rates has important implications for interpreting CSDs in natural volcanic rocks, which have typically assumed constant-rate crystal growth (e.g., Cashman 1988). Thorough testing of CSD models awaits collection of a larger dataset of spherulite growth rates.

CONCLUDING REMARKS

Water concentration profiles around spherulites are quite literally the frozen-in signatures of chemical diffusion driven by phase transformation in silicate melt at high temperature. SFTIR measurements of natural water profiles confirm the genetic relationship between the spherulite growth and volatile enrichment in glassy rhyolite. The shapes of diffusion patterns around spherulites are consistent with combined advective and diffusive transport of water during spherulite growth, followed by a small amount of post-growth diffusion. Diffusion modeling yields spherulite growth rates of a few tenths to hundredths of a millimeter per day, depending on temperature. Diffusion models also suggest that spherulites may grow according to a size-dependent growth mechanism.

REFERENCES

313 Baker, D.R. and Freda, C. (2001) Eutectic crystallization in the undercooled Orthoclase-
314 Quartz-H_2O sytstem: experiments and simulations, European Journal of Mineralogy, 13,
315 453-466.
316 Cashman, K.V. (1988) Crystallization of Mount St. Helens dacite; a quantitative textural
317 approach, Bulletin of Volcanology, 50, 194-209.
318 Castro, J.M., Manga, M., and Martin, M.C. (2005) Vesiculation rates of obsidian domes
319 inferred from H_2O concentration profiles, Geophysical Research Letters, 32, doi
320 10.1029/2005GL020429.
321 Costa, F. and Dungan, M. (2005) Short time scales of magmatic assimilation from
322 diffusion modeling of multiple elements in olivine, Geology, 33, 837-840.
323 Crank, J. (1984) Free and moving boundary problems, 436 p. Clarendon Press, Oxford,
324 UK.
325 Eberl, D.D., Kile, D.E., and Drits, V.A. (2002) On geological interpretations of crystal
326 size distributions: Constant vs. proportionate growth, American Mineralogist, 87, 1235-
327 1241.
328 Frank, F.C. (1950) Radially symmetric phase growth controlled by diffusion.
329 Proceedings of the Royal Society of London, Series A, 201, 586-599.
330 Friedman, I. and Smith, R.L. (1960) A new dating method using obsidian: Part I, The
331 development of the method, American Antiquity, 25, 476-493.
332 Gaillard F., Schmidt, B., Mackwell, S., and McCammon, C. (2003) Rate of hydrogen-
333 iron redox exchange in silicate melts and glasses. Geochimica Cosmochimica Acta 67,
334 2427-2441.

335 Ghiorso, M.S. and Sack, R.O. (1995) Chemical mass transfer in magmatic processes IV:
336 A revised and internally consistent thermodynamic model for the interpolation and
337 extrapolation of liquid-solid equilibria in magmatic systems at elevated temperatures and
338 pressures, Contributions to Mineralogy and Petrology, 119, 197-212.
339 Gonnermann, H. and Manga, M. (2007) The fluid mechanics inside a volcano, Annual
340 Reviews of Fluid Mechanics, 39, 321-356.
341 Gottsmann, J., Giordano, D., and Dingwell, D.B. (2002) Predicting shear viscosity during
342 volcanic processes at the glass transition: a calorimetric calibration, Earth and Planetary
343 Science Letters, 198, 417-427.
344 Gottsmann, J. and Dingwell, D.B. (2001) The cooling of frontal flow ramps: a
345 calorimetric study on the Rocche Rosse rhyolite flow, Lipari, Aeolian Islands, Italy, Terra
346 Nova, 13, 157-154.
347 Granasy, L., Pusztai, T., Gyorgy, T., Warren, J., and Douglas, J. (2005) Growth and form
348 of spherulites. Physical Review, E, 72, 011605.
349 Keith, H.D. and Padden Jr., F.J. (1964) Spherulitic crystallization from a melt. II.
350 Influence of fractionation and impurity segregation on the kinetics of crystallization.
351 Journal of Applied Physics, 35, 1286-1296.
352 MacLellan, H.E. and Trembath, L.T. (1991) The role of quartz crystallization in the
353 development and preservation of igneous texture in granitic rocks: Experimental
354 evidence at 1 kbar. American Mineralogist, 76, 1291-1305.
355 Manley, C. R. (1992) Extended cooling and viscous flow of large, hot rhyolite lavas:
356 implications of numerical modeling results, Journal of Volcanology and Geothermal
357 Research, 53, 27-46.

358 Manley, C.R. and Fink, J.H. (1987) Internal textures of rhyolite flows as revealed by
359 research drilling, Geology, 15, 549-552.
360
361 Newman, S., Stolper, E.M., and Epstein, S. (1986) Measurement of water in rhyolitic
362 glasses: Calibration of an infrared spectroscopic technique, American Mineralogist, 71,
363 1527-1541.
364 Randolf, A.D. and Larson, M.A. (1988) Theory of particulate processes, second edition,
365 New York, Academic Press, 369 pp.
366 Smith, R.K., Tremallo, R.L., and Lofgren, G.E. (2001) Growth of megaspherulites in a
367 rhyolitic vitrophyre, American Mineralogist, 86, 589-600.
368 Sparks, R.S.J. (1997) Causes and consequences of pressurization in lava dome eruptions,
369 Earth and Planetary Science Letters, 150, 177-189.
370 Stasiuk, M.V. Barclay, J., Carroll, M.R., Jaupart, C., Ratte, J.C., Sparks, R.S.J., and Tait,
371 S.R. (1993) Degassing during magma ascent in the Mule Creek vent (USA) Bulletin of
372 Volcanology, 58, 117-130.
373 Stevenson, R.J., Hodder, A.P.W., and Briggs, R.M. (1994) Rheological estimates of
374 rhyolite lava flows from the Okataina Volcanic Centre, New Zealand, 37, 211-221.
375 Swanson, S.E. (1977) Relation of nucleation and crystal-growth rate to the development
376 of granitic textures, American Mineralogist, 62, 966-978.
377 Swanson, S.E., Naney, M.T., Westrich, H.R., and Eichelberger, J.C. (1989)
378 Crystallization history of Obsidian Dome, Inyo Domes, California, Bulletin of
379 Volcanology, 51, 161-176.

Westrich, H.R., Stockman, H.W., and Eichelberger, J.C. (1988) Degassing of rhyolitic magma during ascent and emplacement, Journal of Geophysical Research, 93, 6503-6511.

Wright, F.E. (1915) Obsidian from Hrafntinnuhryggur, Iceland: Its lithophysae and surface markings, Bulletin of the Geological Society of America, 26, 255-286.

Zhang, Y., Stolper, E.M., and Wasserburg, G.J. (1991) Diffusion of water in rhyolitic glasses, Geochimica Cosmochimica Acta, 55, 441-456.

Zhang, Y. and Behrens, H. (2000) H_2O diffusion in rhyolitic melts and glasses, Chemical Geology, 169, 243-262.

ACKNOWLEDGEMENTS

This research was supported by the Alexander von Humboldt Foundation and the U.S. Department of Energy under Contract No. DE-AC02-05CH11231. The comments of Yan Liang, Samuel E. Swanson, and Don Baker are appreciated.

FIGURES

Figure 1. Photomicrographs of spherulites in obsidian. A) spherulites (round, black) viewed in plane polarized light. Matrix is rhyolitic glass of variable oxidation state, providing the different colors. Two SFTIR measurement traverses are shown for reference (profiles OR1305_SPH1_prf1 and 2a). B) Same spherulite as in "A", only viewed in cross-polarized light. Bright fringes are due to strain birefringence from hydration. C) Spherulite in glass matrix showing flow-oriented microlites (slender black rods) deflected around the spherulite. Scale is the same as in "A". D) Back-scattered electron images of spherulites. Interiors consist mostly of plagioclase (pl), an SiO2-polymorph (SiO_2), and magnetite (mt).

Figure 2. A) Backscattered electron image of the internal texture of a spherulite showing energy dispersive spectroscopy (EDS) analysis points. B) Representative EDS spectra of the mineral phases comprising the spherulite pictured in "A". The small Al peak in the SiO2 spectrum arises from contamination from an adjacent feldspar grain. Similarly, the Al and Si peaks in the magnetite are from the electron beam sampling small quantities of adjacent phases.

Figure 3. Water concentration profiles around spherulites in obsidian. The LHS of the diagrams corresponds to spherulite-glass margin, as seen in the subjacent photomicrographs of the corresponding samples.

Figure 4. A) Schematic of a spherulite (*S*) growing and extruding water (H_2O). Vertical dashed lines demarcate the spherulite boundary ($r=r_i$) at a given time ($t>0$); the horizontal dashed line indicates the initial water composition (C_{H2Oi}). B) Comparison of natural concentration data (circles) and diffusion simulations with (solid line) and without (dashed) a 6% post-growth diffusion. C) Model fits to natural data. Shown are a best fit (solid curve) and models run at bracketing growth rates.

Figure 5. A) Logarithm of the best-fit growth timescale versus reciprocal temperature. Linear data arrays reflect Arrhenian dependence of D_{H2O} on temperature. The upper data array represents calculations for two profiles measured on the largest spherulite (OR1305_A; r=730 μm); this spherulite had retained water and thus the results demonstrate the error associated with incomplete extrusion of water during growth. The lower data comprise measurements on four smaller spherulites. B) Average linear growth rate versus spherulite size. The slopes of the linear fits are equal to the inverse growth timescale.

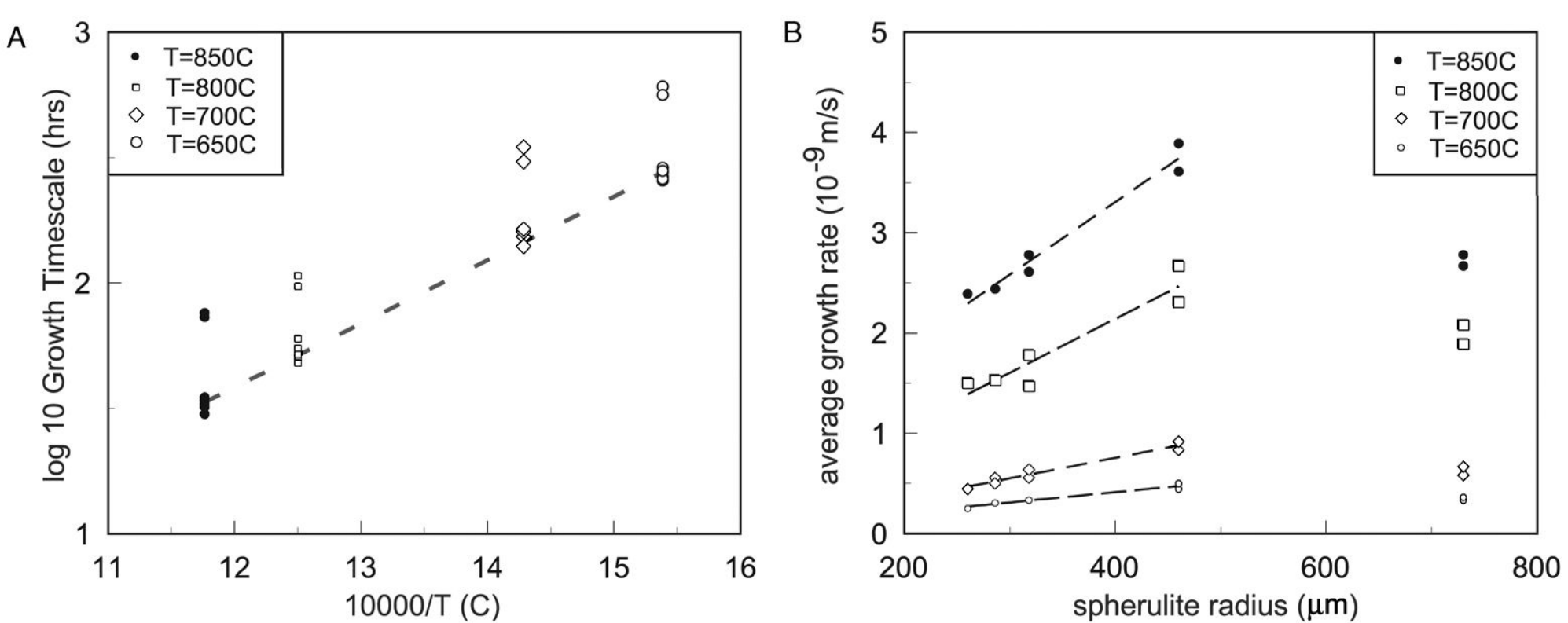

Fig.5., Castro et al.

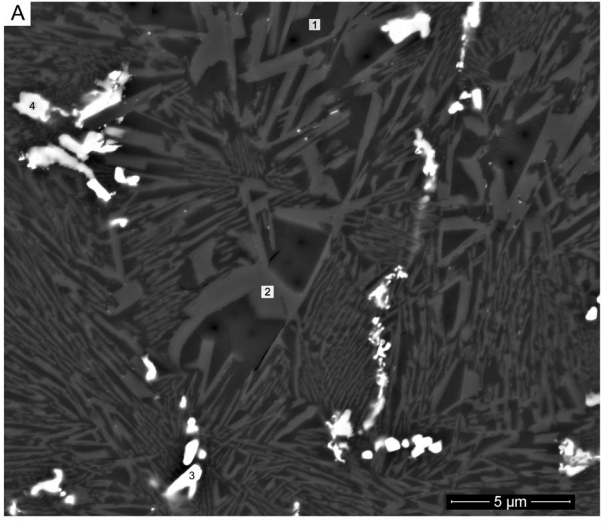

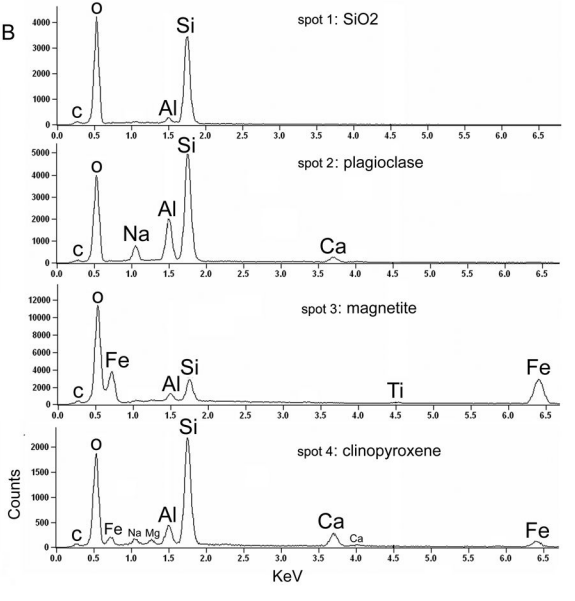

Fig.2., Castro et al.

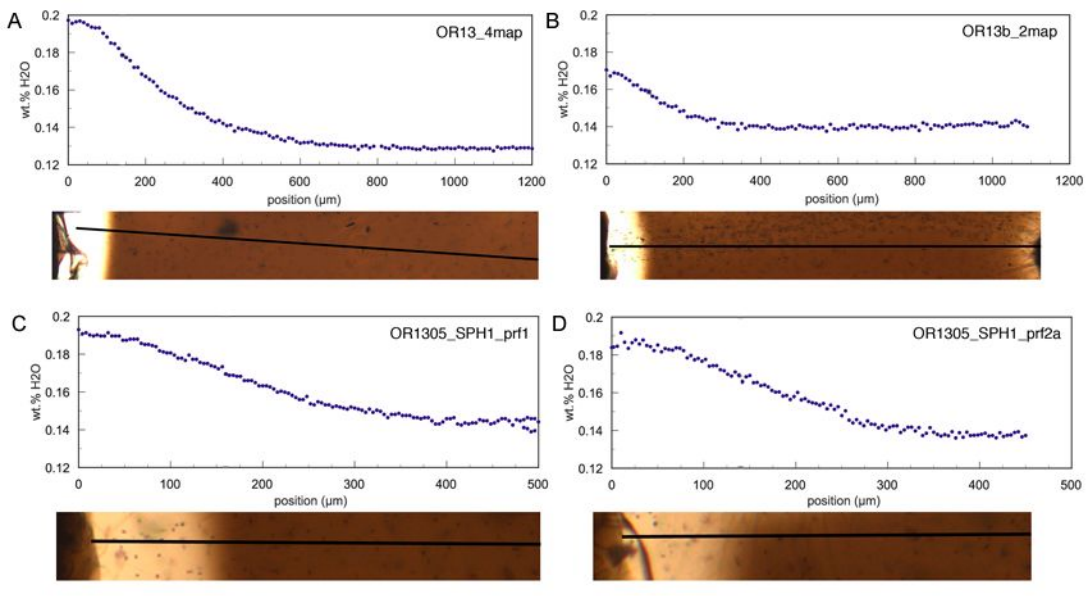

Fig.3., Castro et al.

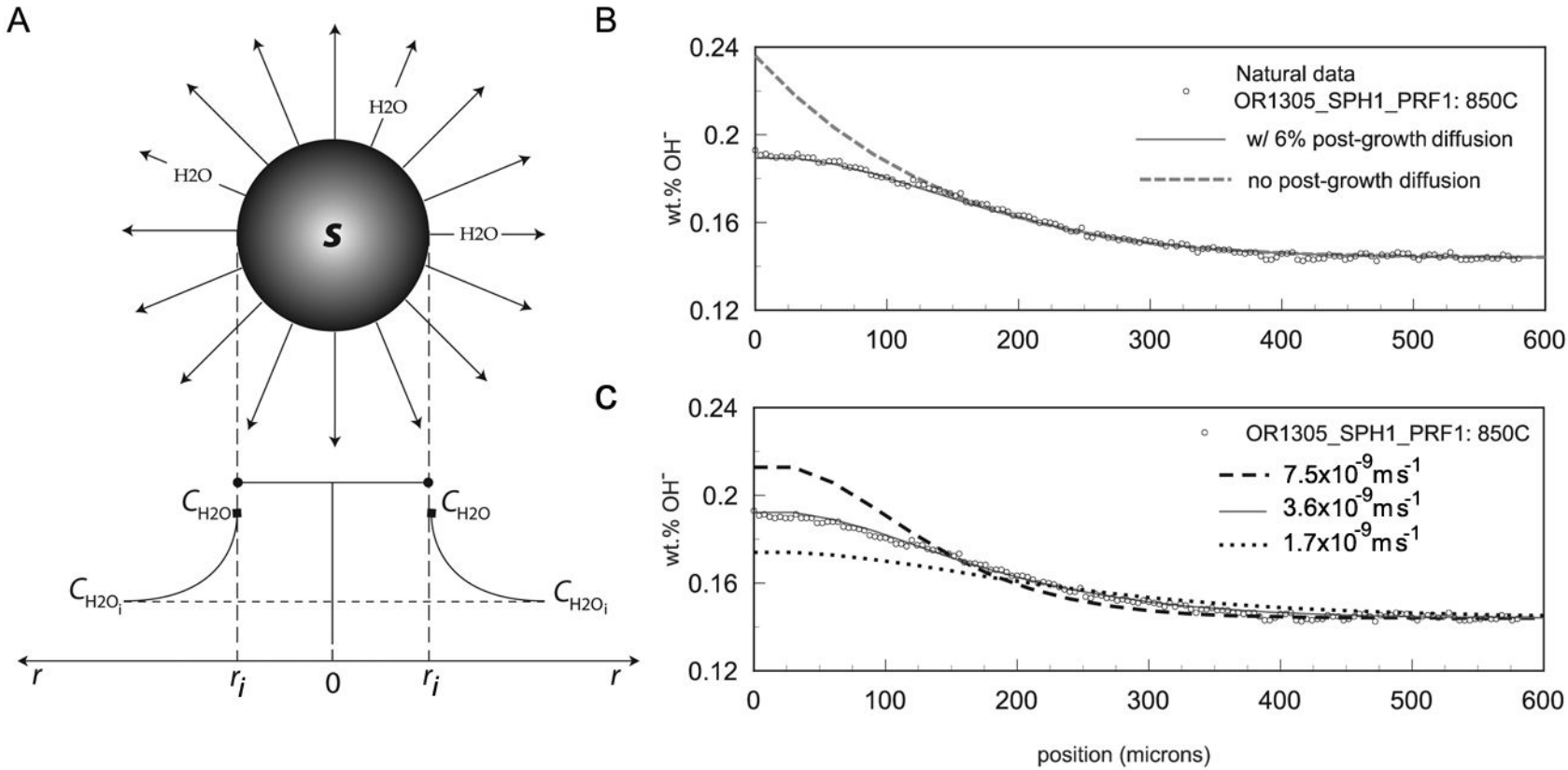

Fig.4., Castro et al.

Table 1. Representative electron microprobe analyses of obsidian from Obsidian Ridge, Krafla volcano

Major oxide wt.% (n=136)		(s.d.)
SiO2	75.0	0.75
TiO2	0.22	0.02
Al2O3	12.0	0.19
FeO	3.23	0.92
MnO	0.11	0.04
MgO	0.1	0.02
CaO	1.68	0.13
Na2O	4.19	0.17
K2O	2.75	0.10
Total	99.3	0.65

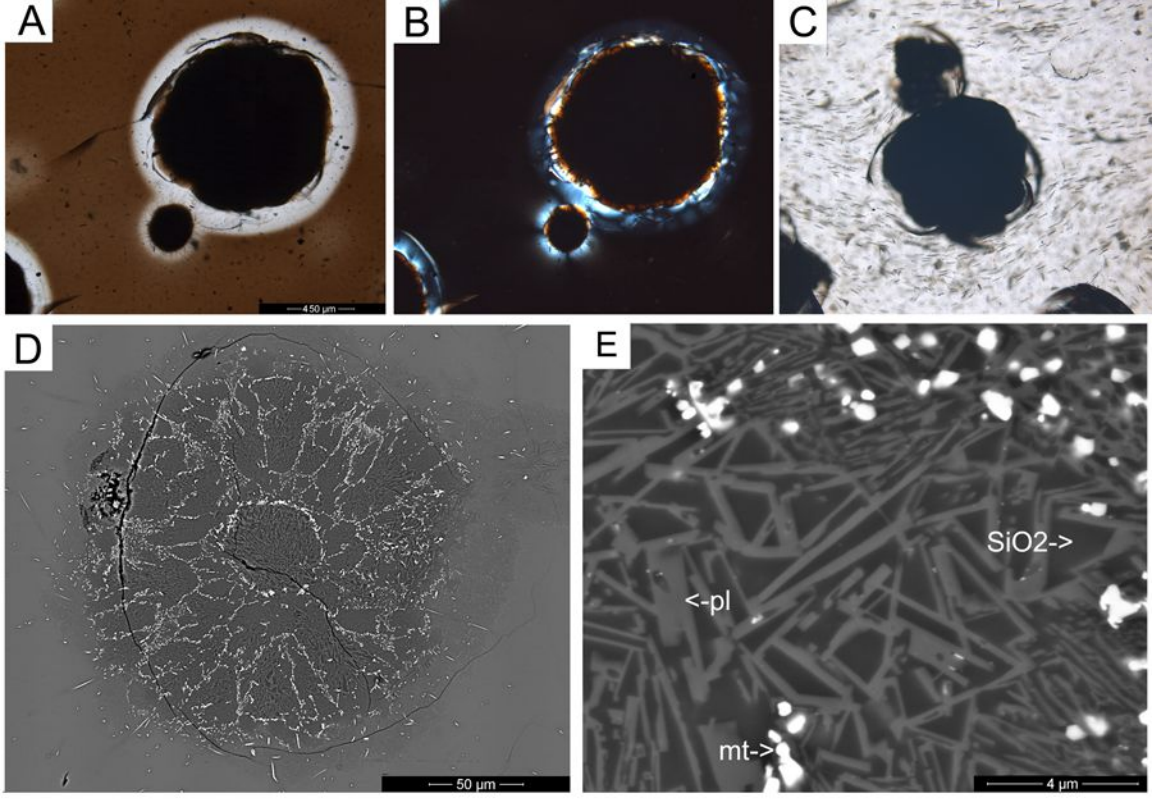

Fig. 1., Castro et al.

Table 2. Properties of water concentration profiles around spherulites

Spherulite	R(µm)*	Prof†	length(µm)§	OH-min**	OH-max***	OH-actual(mg)#	OH-predicted(mg)##
OR1305_A	730	1map	900	0.131	0.195	0.36	0.5
	730	4map	900	0.13	0.197	0.37	0.5
OR1305_SPH1	460	prf1	450	0.134	0.186	0.129	0.129
	460	prf2a	450	0.137	0.188	0.121	0.129
OR1305_D	318	T1map	360	0.132	0.165	0.032	0.042
	318	T2map	380	0.125	0.161	0.041	0.042
OR1305_B	286	2map	370	0.135	0.164	0.029	0.031
	286	3map	350	0.131	0.156	0.028	0.031
OR1305_2	260	2bmap	350	0.131	0.155	0.02	0.023

* spherulite radius
† profile label
§ profile length
** minimum OH^- concentration along profile in wt.%
*** maximum OH^- concentration along profile in wt.%
# amount of water rejected during spherulite growth, measured
amount of water rejected during spherulite growth, predicted

Table 3. Growth timescales (t;hrs)* and rates (G;m/s) determined from diffusion model fits to water concentration profiles.

Profile	t;850˚C	G;850˚C	t;800˚C	G;800˚C	t;700˚C	G;700˚C	t;650˚C	G;650˚C
1map	76(4.6)	2.67E-9	107(6.4)	1.89E-9	348(20.9)	5.83E-10	608(36.5)	3.33E-10
4map	73(4.4)	2.78E-9	97(5.8)	2.08E-9	304(18.2)	6.67E-10	562(33.7)	3.61E-10
prf1	35(2.1)	3.61E-9	55(3.3)	2.31E-9	153(9.2)	8.33E-10	288(17.3)	4.44E-10
prf2a	33(2.0)	3.89E-9	48(2.9)	2.67E-9	140(8.4)	9.17E-10	256(15.4)	5.00E-10
T1map	34(2.0)	2.61E-9	60(3.6)	1.47E-9	160(9.6)	5.56E-10	276(16.6)	3.33E-10
T2map	32(1.9)	2.78E-9	50(3.0)	1.78E-9	140(8.4)	6.39E-10	265(15.9)	3.33E-10
2map	33(2.0)	2.44E-9	52(3.1)	1.53E-9	140(8.4)	5.56E-10	260(15.6)	3.06E-10
3map	33(2.0)	2.44E-9	52(3.1)	1.53E-9	160(9.6)	5.00E-10	260(15.6)	3.06E-10
2bmap	30(1.8)	2.39E-9	48(2.9)	1.50E-9	164(9.8)	4.44E-10	280(16.8)	2.50E-10

*Values in parentheses represent the amount of post-growth diffusion (hrs.) imposed in the model simulations.